Journal of Chemical Physics 158.13 (2023): 134305

DOI: https://doi.org/10.1063/5.0139738

Photoionization of the water molecule with XCHEM

P. Fernández-Milán,[1] V. J. Borràs,[1] J. González-Vázquez,[1] and F. Martín[1, 2, 3, a)]

[1)]*Departamento de Química, Facultad de Ciencias, Universidad Autónoma de Madrid, Madrid, Spain*

[2)]*Instituto Madrileño de Estudios Avanzados en Nanociencia (IMDEA-Nanociencia), Madrid, Spain*

[3)]*Condensed Matter Physics Center (IFIMAC), Universidad Autónoma de Madrid, Madrid, Spain*

(Dated: 13 March 2023)

We have evaluated total and partial photoionization cross sections, β asymmetry parameters, and molecular-frame photoelectron angular distributions (MFPADs) of the water molecule by using the XCHEM methodology. This method accounts for electron correlation in the electronic continuum, which is crucial to describe Feshbach resonances and their autoionization decay. We have identified a large number of Feshbach resonances, some of them previously unknown, in the region between 12.2–18.7 eV, for which we provide energy positions and widths. Many of these resonances lead to pronounced peaks in the photoionization spectra, some of them remarkably wide (up to 0.2 eV, for resonances converging to the third ionization threshold), which should be observable in high-energy resolution experiments. We show that, in the vicinity of these peaks, both asymmetry parameters and MFPADs vary very rapidly with photoelectron energy, which, as in atoms and simpler molecules, reflects the interference between direct ionization and autoionization, which is mostly driven by electron correlation.

[a)]corresponding author: fernando.martin@uam.es

I. INTRODUCTION

In recent years, the development of attosecond XUV pulses has opened the possibility to image and control electron dynamics in molecules[1]. Absorption of a single XUV photon contained in these pulses leads to ionization of any molecular system, so that the light-induced dynamics takes place in molecular cations. Thus, to theoretically investigate such dynamics, one has first to describe the ionization step. In many-electron molecules, besides direct ionization resulting from the absorption of the photon by a single electron, other ionization processes involving more than one electron can take place, e.g., autoionization of multiply excited states embedded in the electronic continuum, Auger decay following ionization of a core electron, or ionization with simultaneous electronic excitation of the resulting cation (shakeup). All these processes would not be possible without electron-electron interactions. Therefore, to describe them, theoretical methodologies[2–7] must account for electron correlation in the molecular continuum, which, in general, is not a trivial matter. XCHEM[7,8] is one these methods. It has been successfully applied to atomic systems, like hydrogen[7], helium[7], neon[9,10] and argon[11], and diatomic molecules, like hydrogen[7], nitrogen[12], oxygen[13] and carbon monoxide[14]. In this paper, we apply it for the first time to photoionization of a triatomic molecule, water, in the region of photon energies where Feshbach resonances are expected to appear, i.e., where correlation effects in the electronic continuum cannot be ignored.

Photon driven processes in the water molecule are relevant in diverse areas such as astrophysics, biology, radiation chemistry and catalysis. In particular, the ionization-induced dynamics in water is important, because it initiates the processes that lead to DNA damage[15,16] and eventually to cell death, with clear implications in medical therapy. Total and partial photoionization cross sections for the water molecule have been measured in the 70s and 80s by using synchrotron radiation[17–19] and (e, 2e) spectroscopy[20,21]. Recently, by using the most advanced experimental techniques in attosecond science, photoionization time delays have been measured in the water molecule and in clusters of water molecules[22,23], and the role of electron-hole delocalization in such delays has been discussed. Several theoretical studies on H_2O photoionization have already been reported[6,24–27], mainly in regions where Feshbach resonances are not expected to appear. With the exception of the work of Ref.[25], all calculations were performed in the fixed-nuclei approximation by assuming that the molecule is at its equilibrium geometry. As shown by these works, this is a reasonable approximation to interpret experiments in which vibrationally resolved information is not accessible, which is the case of all previously reported experiments. Some

theoretical works have also investigated the role of Rydberg states lying below the first ionization threshold[17,28–31]. However, with the exception of the early work of Dierckersen *et al*. .[24], in which the positions of Feshbach resonances lying above the first few ionization thresholds were obtained, no systematic theoretical study of water photoionization in this energy region has been reported so far. Here, we aim at partially filling this gap.

In this work, we have evaluated total and partial photoionization cross sections, β asymmetry parameters, and molecular-frame photoelectron angular distributions (MFPADs) of the water molecule, by using the XCHEM methodology[7] and its recent extension to MFPADs[14]. As in most previous theoretical work on this molecule, we have made use of the fixed-nuclei approximation, since simultaneous inclusion of nuclear motion and electron correlation effects in the vicinity Feshbach resonances is prohibitively expensive for water (in fact this has only been achieved for the simplest of all molecules, H_2; see, e.g.,[32,33]). We have focused our attention on the region between the first and third ionization thresholds, which is brimming with Feshbach resonances. As expected, many of these resonances lead to pronounced peaks in the photoionization spectra, some of them remarkably wide (up to 0.2 eV, for resonances converging to the third ionization threshold), which reflect their very short lifetime and should thus be observable in real experiments, i.e., where the nuclei move. We show that, in the vicinity of these peaks, both asymmetry parameters and MFPADs vary very rapidly with photoelectron energy, which, as in atoms and simpler molecules, reflects the interference between the direct ionization and autoionization processes. Finally, we provide a set of energy positions and autoionization widths for the most relevant resonances found in our calculations.

The paper is organized as follows. The theoretical methodology is described in section II, the computational details in section III and results are presented and discussed in section IV. We end with some conclusions in section V.

II. THEORY

A. The XCHEM methodology

The XCHEM methodology has been introduced in detail in previous work[7,34], so here we only describe the basic concepts. XCHEM uses a hybrid Gaussian–B-spline basis (GABS)[34] combining the usual basis used in bound state calculations, but unsuited to describe the continuum, with a B-

spline basis that provides a good description of the highly oscillating continuum wave functions. In XCHEM, a polycentric Gaussian basis coming from standard Quantum Chemistry packages is coupled with the set of B-spline functions via a monocentric Gaussian basis that totally envelops the polycentric basis. The B-spline functions are placed at a distance R_0, far enough from the center of mass of the molecule, so that the overlap with the polycentric basis can be neglected.

The XCHEM continuum wave function $\Psi_{\alpha E}$ is written in the Close Coupling formalism as

$$\Psi_{\alpha E}(\boldsymbol{x}_1 \dots \boldsymbol{x}_N) = \sum_i c_{i\alpha E}\, \aleph_i(\boldsymbol{x}_1 \dots \boldsymbol{x}_N) + \sum_{\beta i} c_{\beta i,\alpha E} \bar{\Upsilon}_{\beta i}(\boldsymbol{x}_1 \dots \boldsymbol{x}_N) \tag{1}$$

where $\boldsymbol{x}_i$ are the spin and position of electron i. We distinguish two terms. The first one includes short-range states $\aleph_i$ where all N electrons are within a radius R_0 from the center of mass of the molecule. They are purely described by Gaussian functions. The second term consists of a linear combination of extended channel functions $\bar{\Upsilon}_{\alpha i}$ defined as

$$\bar{\Upsilon}_{\alpha i}(\boldsymbol{x}_1 \dots \boldsymbol{x}_N) = N_{\alpha i} \hat{A} \Upsilon_\alpha(\boldsymbol{x}_1 \dots \boldsymbol{x}_{N-1}; \hat{r}_N, \zeta_N) \rho_i(r_N) \tag{2}$$

where $\hat{A}$ is the antisymmetrizer, Υ_α is a channel function constructed by coupling a $(N-1)$-electron parent ion state Φ_a with the spin of the N-th electron (continuum), multiplied only by the angular wave function of the N-th electron; red$\hat{r}_N$ are the angular coordinates of electron N, ζ_N is the spin of electron N, and ρ_i is a radial one-electron function describing the photoelectron in the continuum. In XCHEM it takes the form of a Gaussian or a B-spline function, as depicted fig. 1 and as we will shortly see in section III.

From the short-range states and the extended channel functions, the matrix representations of the Hamiltonian and other operators are constructed[7]. In fig. 1 we show a block representation of the Hamiltonian matrix for the channel functions Υ_α. We can see that the short-range states do not interact with channel functions when they are extended with a B-spline function and that the total Hamiltonian matrix is actually composed of several of these blocks, one for each channel function, which in general are not orthogonal to each other. This is one of the computational advantages of XCHEM when compared to other methods that make use of gaussian and B-spline functions, since in XCHEM one does not have to explicitly calculate integrals involving polycentric gaussian and monocentric B-spline functions, which are not analytical.

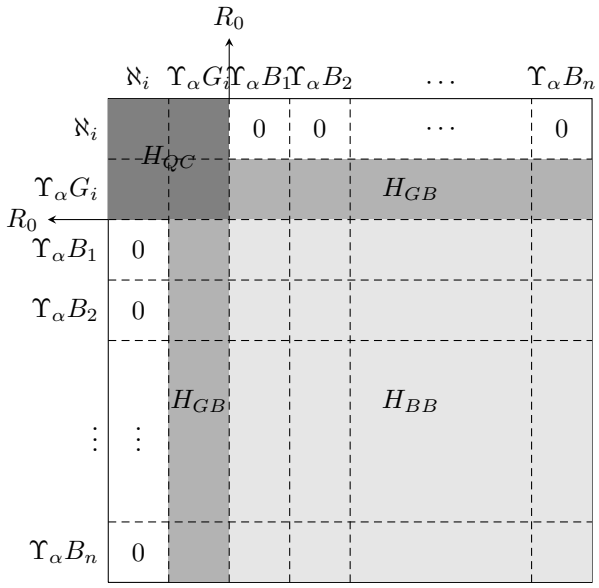

FIG. 1. Structure of the Hamiltonian matrix for a given channel function Υ_α. The H_{QC} block involves only the short-range states $\aleph_i$ and Gaussian function augmentations states $\Upsilon_\alpha G_i$. The short-range states $\aleph_i$ in this block are not coupled to the states resulting from augmenting with a B-spline function. H_{GB} is the coupling between Gaussian augmentation states and B-spline augmentation states. H_{BB} is the coupling between B-spline functions and gives rise to a sparse matrix block.

B. Resonance analysis

To characterize the electronic structure of the Feshbach resonances observed in the photoionization spectra, which is essential for a correct labeling, in this work we have implemented a method that allows us to obtain a "Rydberg orbital" representation of the outer bound electron in those resonances. The method only considers the augmented Gaussian part of the Hamiltonian H_{QC} for each parent ion separately. This means that we construct a submatrix from all the channel functions augmented with a Gaussian associated with a specific parent ion. By diagonalizing this subset of the total Hamiltonian we obtain the bound states Ψ_i associated with a given parent ion, which have the following form:

$$|\Psi_i\rangle = \sum_j c_j a_j^\dagger |\Phi_a\rangle = \sum_j c_j |\Phi_a\rangle G_j \tag{3}$$

where $|\Phi_a\rangle$ is a parent ion state, $a_j^\dagger$ is the creation operator and G_j is a Gaussian orbital. The bound states Ψ_i are linear combinations of augmented parent ion states with one electron in a Gaussian

orbital. By factoring out $|\Phi_a\rangle$

$$|\Psi_i\rangle = |\Phi_a\rangle \sum_j c_j G_j \tag{4}$$

we can see that the states Ψ_i are products of a parent ion state and a linear combination of Gaussian orbitals. The latter can be interpreted as the Rydberg orbital that contains the outer electron in the resonance before it autoionizes.

We compute the dipole transition amplitude between each of these Ψ_i states and the ground state. For a given resonance in the photoionization spectrum, we look for the eigenstate resulting from the diagonalization of H_{QC} (in the augmented Gaussian part) with an energy very close to that of the resonance peak and with a high value of the dipole transition amplitude for the polarization direction at which the resonance is active. The Rydberg orbital associated with this eigenstate, defined as above, will then be used to label the resonance. Since we are only considering the Gaussian part of the Hamiltonian, this method is only suited for Rydberg states far from the ionization threshold, where the contribution of the B-spline functions can be safely neglected.

III. COMPUTATIONAL DETAILS

In this work, we consider the nuclei fixed at the equilibrium geometry obtained from an MP2 optimization ($r_{O-H} = 0.959056$ Å, $\widehat{HOH} = 103.512^\circ$). The water molecule has a closed-shell structure with the following ground state electronic configuration: $(1a_1)^2(2a_1)^2(1b_2)^2(3a_1)^2(1b_1)^2$. We assume that, after photoionization, the water cation can only be left in one of its three lowest electronic states $\tilde{X}\ ^2B_1$, $\tilde{A}\ ^2A_1$ and $\tilde{B}\ ^2B_2$. These states can approximately be seen as one-hole states[24] that arise from the removal of an electron from the $1b_1$, $3a_1$ and $1b_2$ molecular orbitals, schematically shown in fig. 2. In order to accurately represent the corresponding ionization potentials, first we have obtained a set of orbitals from a state-averaged CAS-SCF calculation over different symmetries using MOLPRO[35]. In this calculation, we have included the water neutral ground state $\tilde{X}\ ^1A_1$ and the cation states $\tilde{X}\ ^2B_1$, $\tilde{A}\ ^2A_1$ and $\tilde{B}\ ^2B_2$. We have used a cc-pVTZ[36] basis set. Then, we have performed calculations by using an active space CAS(8, 8) that includes $2a_1$, $1b_2$, $3a_1$, and $1b_1$ as occupied orbitals, and $4a_1$, $2b_2$, $2b_1$ and $5a_1$ as virtual orbitals (see also fig. 2). The used active space gives ionization potentials close to the experimental values, see table I. They also compare reasonably well with those calculated in[26]. We note that, although some of the primitive gaussian functions in the polycentric cc-pVTZ basis may be very diffuse, they are multiplied by contraction coefficients to form the contracted gaussian functions, which, in turn,

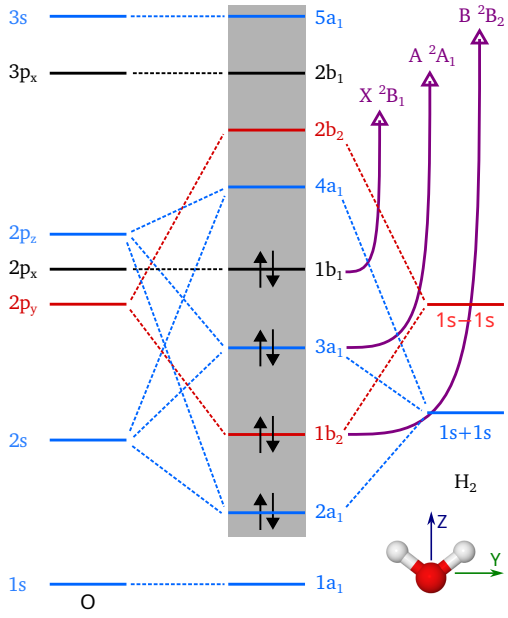

FIG. 2. Schematic molecular orbital diagram of H_2O and the corresponding electron removals that give rise to the cation states $\tilde{X}\,^2B_1$, $\tilde{A}\,^2A_1$ and $\tilde{B}\,^2B_2$. Different orbital symmetries appear with different colors: (blue) a_1, (red) b_1 and (black) b_2. The gray background contains the orbitals included in the active space. The orientation of the water molecule is also shown, with the z axis coinciding with the C_2 rotation axis.

are also multiplied by a coefficient when forming the molecular orbitals. Thus, if the molecular orbitals are not extremely diffuse, the contribution of those primitive gaussians is actually quite low so that the block structure on the Hamiltonian shown in Fig. 1 remains valid.

The polycentric gaussian basis used in the electronic structure calculation is then augmented with the GABS basis described in section II. The Gaussian part is made up of a set of 22 even-tempered gaussian functions of the form $G_i(r) \propto r^{l+2k} e^{-\alpha_i r^2}$ for each l, m and k. Unless otherwise stated, all the results herein presented have used an angular momentum up to $l_{\max} = 4$ and $k \leq 1$ for all l values. The gaussian exponents α_i are taken from the even tempered progression $\alpha_i = \alpha_0 \beta^i$ where $\alpha_0 = 0.01$ and $\beta_0 = 1.46$ for $i = 0, 1, \ldots, 21$, values already used in previous XCHEM works[9,12–14]. The monocentric gaussian basis set consists thus of a total of 1100 primitive gaussian functions that make up 664 linearly independent gaussian orbitals. The B-spline region comprises a box with 380 B-spline nodes of order 7 that ranges from $R_0 = 8.0$ au to $R_{max} = 200$ au. As the ground state is highly localized, it is actually not necessary to use such a large radial extent, but it would probably be necessary in pump-probe calculations in which continuum-continuum transitions are involved.

TABLE I. Ionization potentials in eV. The present XCHEM results are compared with those obtained with UKRmol[26] and with the experimental values reported by Potts *et al.*[37] and Brundle *et al.*[38].

Cation	XCHEM	UKRmol	Potts *et al.*	Brundle *et al.*
$\tilde{X}\ ^2B_1$	12.21	12.82	12.61	12.6
$\tilde{A}\ ^2A_1$	14.51	15.18	14.74	14.7
$\tilde{B}\ ^2B_2$	18.73	19.35	18.55	18.5

In this work we focus on the energy region between the first and third ionization thresholds, i.e., from 12.2 to 18.7 eV. In this energy region, the electronic continua starting at the $\tilde{X}\ ^2B_1$ and $\tilde{A}\ ^2A_1$ ionization thresholds are full of Feshbach resonances, see fig. 3, which arise from Rydberg states converging to the $\tilde{A}\ ^2A_1$ and $\tilde{B}\ ^2B_2$ ionization thresholds. Our calculations do not consider cationic states above the $\tilde{B}\ ^2B_2$ one, therefore no resonances are expected to appear above 19 eV.

IV. RESULTS

A. Convergence tests and comparison with previous work

As mentioned above, in this work we focus on the energy region 12.2–18.7 eV. Therefore, all convergence tests have been performed in this region. Here one expects to see the signature of Feshbach resonances lying below the third ionization threshold of water. In general, these resonances should show up as asymmetric peaks, as they reflect the interference between direct non-resonant photoionization and autoionization from Rydberg states embedded in an electronic continuum. These interferences are very sensitive to small deficiencies in the description of electron correlation.

We have checked the convergence with angular momentum and the gauge invariance of the partial photoionization cross sections in the $\tilde{X}\ ^2B_1$ and $\tilde{A}\ ^2A_1$ channels, see fig. 3. For this, we have performed additional XCHEM calculations with maximum angular momentum $l_{\max} = 6$, i.e., higher than $l_{\max} = 4$, the value chosen to obtain all results shown below. As can be seen, the results for $l_{\max} = 4$ and $l_{\max} = 6$ are nearly identical in both length and velocity gauges, meaning that our calculations are well converged in terms of angular momentum. Furthermore, the results obtained in the length and velocity gauges are very similar: the curves are parallel and close to each other,

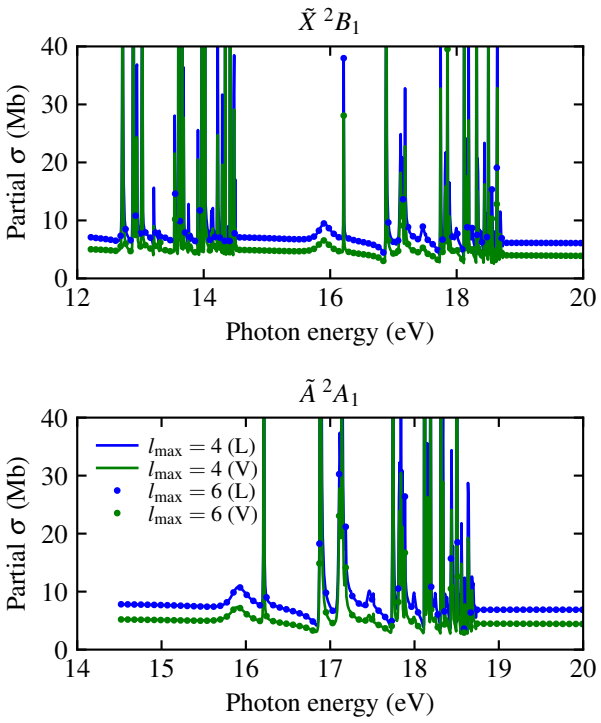

FIG. 3. Orientation averaged partial cross sections for single-photon ionization of H_2O obtained from two XCHEM calculations with different angular momentum basis in the energy region between 12 and 19 eV. Top panel: partial ionization cross section for leaving the ion in the $\tilde{X}\ ^2B_1$ state. Bottom panel: Same for the $\tilde{A}\ ^2A_1$ state. Blue: length gauge. Green: velocity gauge. Solid line: $l_{max} = 4$. Dots: $l_{max} = 6$.

showing the same features at exactly the same spots.

Before driving our attention to the resonances seen in this low energy region, it is interesting to compare our calculated cross sections and asymmetry parameters with the available experimental results, which have been obtained at higher photon energies or have only reported a few values in the energy region considered in the present work. At the same time, we will compare with the results of previous theoretical calculations. In fig. 4, we compare the orientation-averaged total photoionization cross section of H_2O obtained from XCHEM with the available experimental data[39,40] and the calculated results from UKRmol[26] up to 40 eV photon energy. The few available experiments below 20 eV do not have enough resolution to resolve the resonances. Nonetheless, we see that, on average, the description given by XCHEM in this energy region is compatible with the few available experimental points. In both XCHEM and UKRmol calculations, the cross section increases substantially after every new ionization channel opens. Near 20 eV, the XCHEM length gauge result compares quite well with the UKRmol one (which was also obtained in the

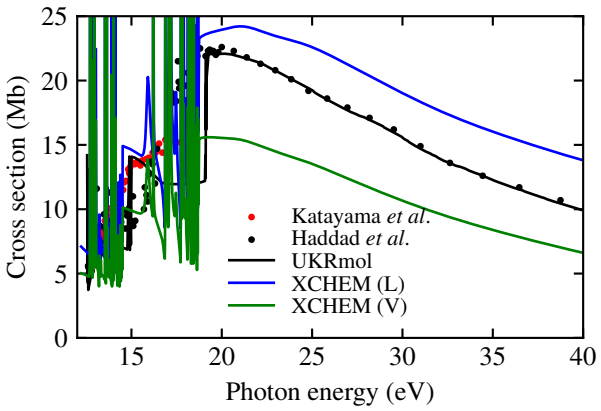

FIG. 4. Total cross section for single-photon ionization of H_2O obtained with XCHEM in length (blue line) and velocity (green line) gauges compared to experimental data from Katayama *et al.*[39] and Haddad *et al.*[40], and theoretical results from UKRmol[26] in length gauge (grey line).

length gauge) and the experimental data, but, as the photon energy increases, it deviates, which is probably the consequence of having chosen basis sets that only ensure good convergence in the low energy region, in particular convergence of all resonant features. For the same reason, gauge invariance above 18.5 is worse than at lower energies.

We have also computed the partial photoionization cross section for each individual channel $\tilde{X}\ ^2B_1$, $\tilde{A}\ ^2A_1$ and $\tilde{B}\ ^2B_2$, see fig. 5, and compared them with the experiments of Banna *et al.*[19], Truesdale *et al.*[18], Tan *et al.*[20] and Brion *et al.*[21] and against the CIS method of Toffoli *et al.*[6] and the smoothed UKRmol results[26]. For the $\tilde{X}\ ^2B_1$ channel, we also show the results obtained by Engin *et al.*[25] by using an extension of the static-exchange density functional theory. The agreement with experiment and other methodologies up to 40 eV is reasonable, even though our calculations were designed for photoionization at lower energies. Gauge invariance at the higher energies is also reasonable, with the experimental data lying in between the length and velocity results, except for the results by Brion *et al.*[21], which lie above the XCHEM ones and the other theoretical results for photon energies below 20 eV.

In fig. 6, we show the computed β asymmetry parameters and compare them with previous experimental and theoretical data. The results obtained with XCHEM are in very good agreement with the experimental data and previous theoretical work. The XCHEM velocity gauge reproduces perfectly the asymmetry parameters for all three channels considered. The length gauge, on the other hand, deviates at a photon energy of $\sim$30 eV for the channels $\tilde{X}\ ^2B_1$ and $\tilde{A}\ ^2A_1$. Again, the

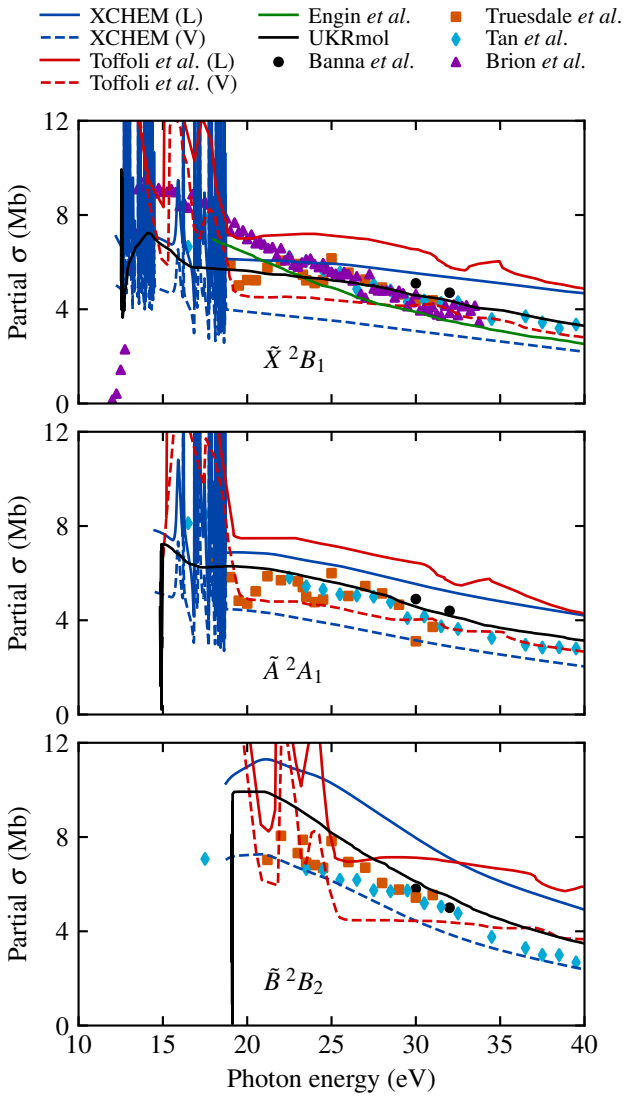

FIG. 5. Partial cross sections for single-photon ionization of H_2O for the three lowest ionization channels $\tilde{X}\ ^2B_1$, $\tilde{A}\ ^2A_1$ and $\tilde{B}\ ^2B_2$. XCHEM results are compared with existing theoretical and experimental results. The experimental data come from Banna *et al.*[19], Truesdale *et al.*[18], Tan *et al.*[20] and Brion *et al.*[21], and are shown as circles, squares, diamonds and triangles, respectively. The theoretical results correspond to (solid and dashed blue lines) XCHEM, (solid and dashed red lines) CIS method from Toffoli *et al.*[6], (solid green line) Engin *et al.*[25] and (solid black line) UKRmol[26].

reason for this discrepancy is likely due to our optimization of the basis parameters to accurately represent the low energy region. The channel $\tilde{B}\ ^2B_2$ is perfectly reproduced by both gauges with an excellent agreement. In the resonance region, we can see that the β parameter changes abruptly, indicating that the MFPADs must also suffer from abrupt changes when a resonance is populated,

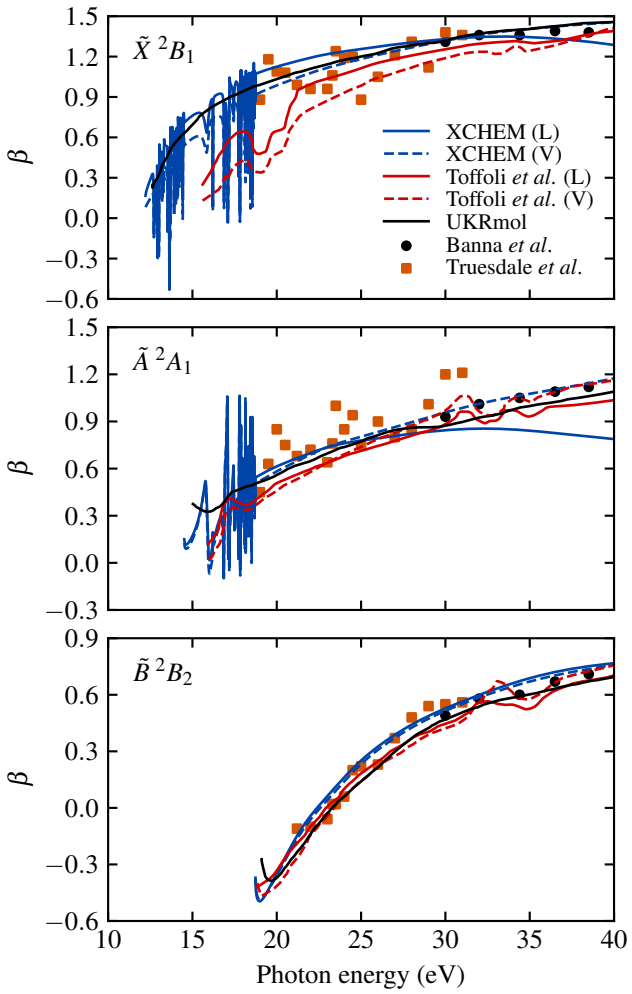

FIG. 6. Asymmetry parameter for single-photon ionization of H_2O for the three lowest ionization channels $\tilde{X}\ ^2B_1$, $\tilde{A}\ ^2A_1$ and $\tilde{B}\ ^2B_2$. XCHEM results are compared with existing theoretical and experimental results. The experimental data come from (circles) Banna *et al.*[19] and (squares) Truesdale *et al.*[18]. The theoretical results correspond to (solid and dashed blue lines) XCHEM, (solid and dashed red lines) CIS method from Toffoli *et al.*[6] and (solid black line) UKRmol[26].

as we will see below.

The good agreement between our results and the experimental results up to a photon energy of 40 eV, for both partial photoionization cross sections and β parameters, further supports the appropriateness of the present calculations, even though they were designed to study photoionization in the energy region below 20 eV.

It is worth mentioning that to improve our description at the higher energies, one should include more ionization channels in the close-coupling expansion, as more and more of these channels

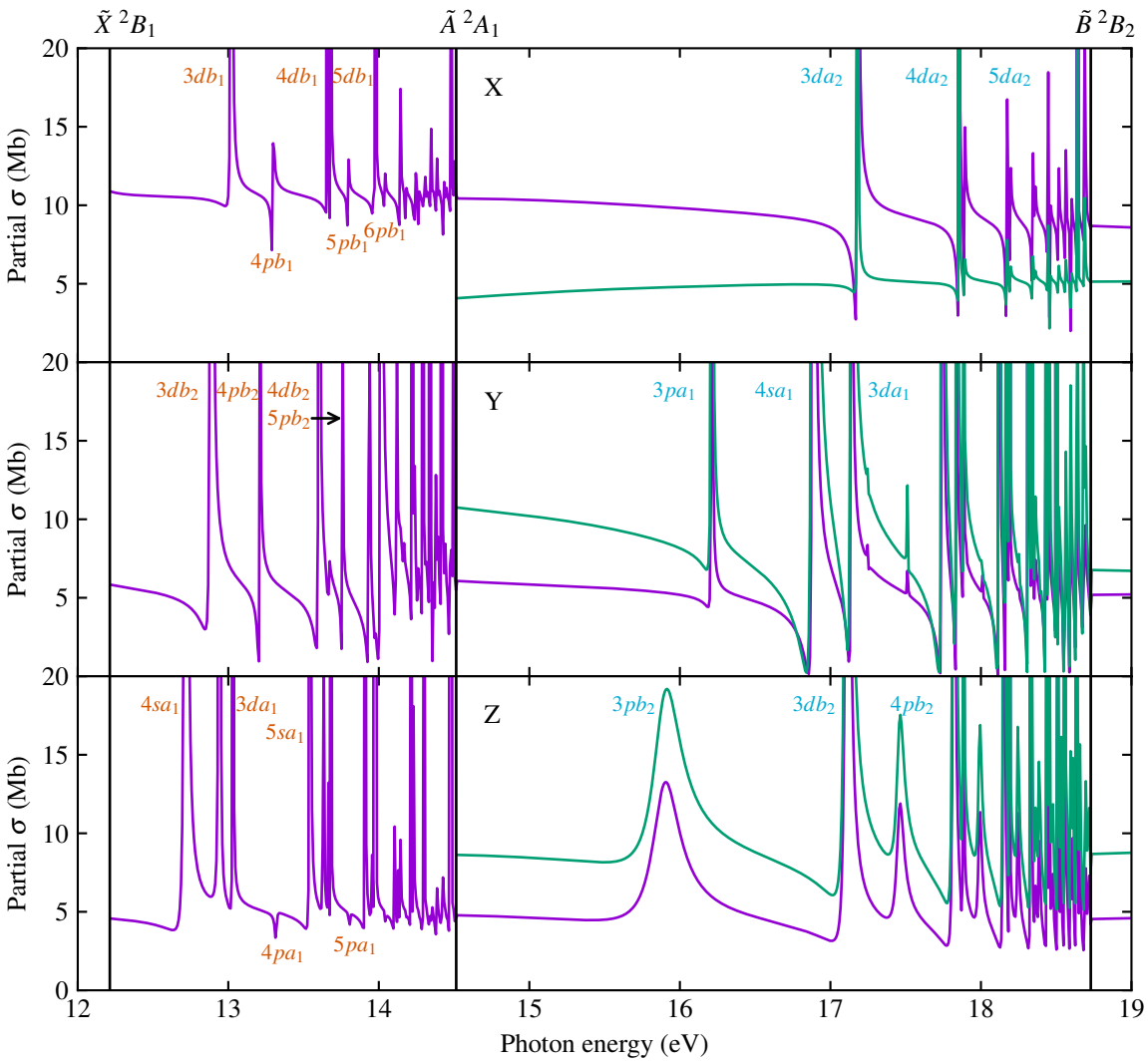

FIG. 7. Partial cross sections for (purple line) $\tilde{X}\,^2B_1$ and (green line) $\tilde{A}\,^2A_1$ ionization channels in the energy region 12–19 eV, calculated with XCHEM in length gauge. Top, middle and bottom panels: partial cross sections for polarization along the x, y and z directions, respectively. Labels of autoionizing states converging to the $\tilde{A}\,^2A_1$ threshold are indicated in orange and those converging to $\tilde{B}\,^2B_2$ in blue.

become accessible. However, in such case, using active spaces as large as those employed in the present work would be computationally very expensive. Consequently, one should reduce the size of the active spaces, thus significantly deteriorating the quality of the resonances' description. Nevertheless, using reduced active spaces at higher energies should not be a serious drawback since Feshbach resonances are never observed at high energies.

B. Photoionization at low photon energies

We now focus on the region between the first and third ionization thresholds, i.e., 12.21–18.73 eV. In this region, Feshbach resonances associated with Rydberg states converging to the $\tilde{A}\,^2A_1$ and $\tilde{B}\,^2B_2$ thresholds are expected to appear. In fig. 7, we show the partial photoionization cross sections for the $\tilde{X}\,^2B_1$ and $\tilde{A}\,^2A_1$ channels and for x, y and z polarizations. The second ionization threshold divides this region into two parts. In the first one, only the $\tilde{X}\,^2B_1$ channel is open for ionization and the resonances come mainly, but not exclusively, from autoionizing states converging to the $\tilde{A}\,^2A_1$ threshold. The orange labels in this first part refer to the Rydberg orbital associated with the outer electron in this series of autoionizing states. This has been determined as described in section IIB. In the second part, above 14.51 eV, the $\tilde{A}\,^2A_1$ channel is open for ionization as well, and all the resonances correspond to Rydberg states converging to the $\tilde{B}\,^2B_2$ threshold. The blue labels indicate the Rydberg orbital of the outer electron. Figure 7 clearly shows several nl series, e.g., ndb_1, npb_1 and nda_2 in x polarization; ndb_2 and npb_2 in y polarization; and nsa_1, npa_1 and npb_2 in z polarization. The resonance peaks that belong to the same nl series exhibit a similar shape, with decreasing width as they approach the upper ionization threshold.

We have determined the energy positions and widths of the assigned resonances in fig. 7. They have been obtained by fitting the total scattering phase[41] to the expression

$$\delta(E) = \delta_b(E) + \arctan\frac{\Gamma_n}{2(E-E_n)} \tag{5}$$

where E_n is the energy position of the resonance, Γ_n is the resonance width and δ_b is a background, approximated in our case by a second order polynomial as a function of the energy.

The fitted energies and widths are given in tables II and III for autoionizing states converging to the $\tilde{A}\,^2A_1$ and $\tilde{B}\,^2B_2$ thresholds, respectively. In both tables we have included the energies calculated by Diercksen *et al*.[24] and the shape of the approximate Rydberg orbitals (i.e., considering only the Gaussian part, see above). In general, our calculated energy positions are in good agreement with those of Diercksen *et al*. For autoionizing states converging to the $\tilde{A}\,^2A_1$ threshold (table II) our energies are slightly below those of Diercksen *et al*. , while for autoionizing states converging to the $\tilde{B}\,^2B_2$ threshold they are slightly above. Most of the resonances we have calculated are quite narrow, hence they have very long lifetimes and may not show up in photoionization spectra due to nuclear motion, even with very high energy resolution. In this respect, it is important to mention that, in the case of the nitrogen molecule, resonances with widths of 1 meV or more have been seen experimentally by using synchrotron radiation with high-energy resolution.[42–46].

TABLE II. Energy positions and autoionization widths for Feshbach resonances converging to the $\tilde{A}\ ^2A_1$ threshold obtained by fitting the scattering eigenphase to eq. (5). The calculated energies are compared with those obtained by Diercksen *et al.*[24]. We show views along the x, y and z axes of the Rydberg orbitals associated with each resonance, as explained in section II B. The corresponding labels are shown in orange color in fig. 7.

Resonance	**Energy (eV)**	**Widths (meV)**	**Diercksen (eV)**	**X view**	**Y view**	**Z view**
$4sa_1$	12.717	11.33	12.77			
$5sa_1$	13.543	3.83	13.67			
$6sa_1$	13.910	1.63	14.07			
$3db_2$	12.886	2.81	13.13			
$3da_1$	12.941	1.41	13.14			
$3db_1$	13.020	2.60	13.25			
$4db_1$	13.679	0.90	13.88			
$5db_1$	13.979	0.48	14.18			
$3da_1$	13.030	2.71	13.23			
$4pb_2$	13.208	3.07	13.35			
$4pb_1$	13.297	3.29	13.45			
$5pb_1$	13.796	1.36	13.97			
$6pb_1$	14.039	0.74	13.97			
$4pa_1$	13.317	13.72	13.51			
$5pa_1$	13.804	6.15	13.99			
$6pa_1$	14.044	3.24	14.30			

TABLE III. Same as in table II but for Feshbach resonances converging to the $\tilde{B}\,^2B_2$ threshold. The resonance labels based on the Rydberg orbitals are shown in blue color in fig. 7.

Resonance	Energy (eV)	Widths (meV)	Diercksen (eV)	X view	Y view	Z view
$3pb_2$	15.888	219.45	15.77			
$4pb_2$	17.457	58.23	17.27			
$3pa_1$	16.212	3.14	15.97			
$4sa_1$	16.885	7.63	16.47			
$3db_2$	17.112	29.38	17.04			
$3da_2$	17.180	2.12	17.03			
$4da_2$	17.854	0.88	17.70			
$5da_2$	18.170	0.46	18.01			

Nuclear motion in H_2O involves hydrogen atoms, which are much lighter than nitrogen atoms and therefore can move faster and farther, so we do not expect that resonances with widths of the order of 1 meV will show up in actual photoionization spectra. Even so, in absorption experiments by Gürtler *et al.*[17] the Rydberg state $1b_2^{-1}4sa_1$ has been observed to lie between 16 and 17 eV, and the state $3a_1^{-1}4sa_1$ at $\sim$12.9 eV. In our calculations these states appear at 16.885 eV (see table III) and 12.717 eV (see table II), being thus in good agreement with experiment. Both resonances have a width of the order of 10 meV according to our calculations.

It is worth focusing our attention on the $1b_2^{-1}3pb_2$ resonance appearing at 15.888 eV, which has a width of 219.45 meV. This width corresponds to a very short lifetime, of the order of 3 fs. This is much shorter than the time needed by the nuclei to move significantly. The same applies to the other members of the $1b_2^{-1}npb_2$ series, since they also have rather large autoionization widths. Therefore, these resonances are good candidates to be observed in photoionization experiments.

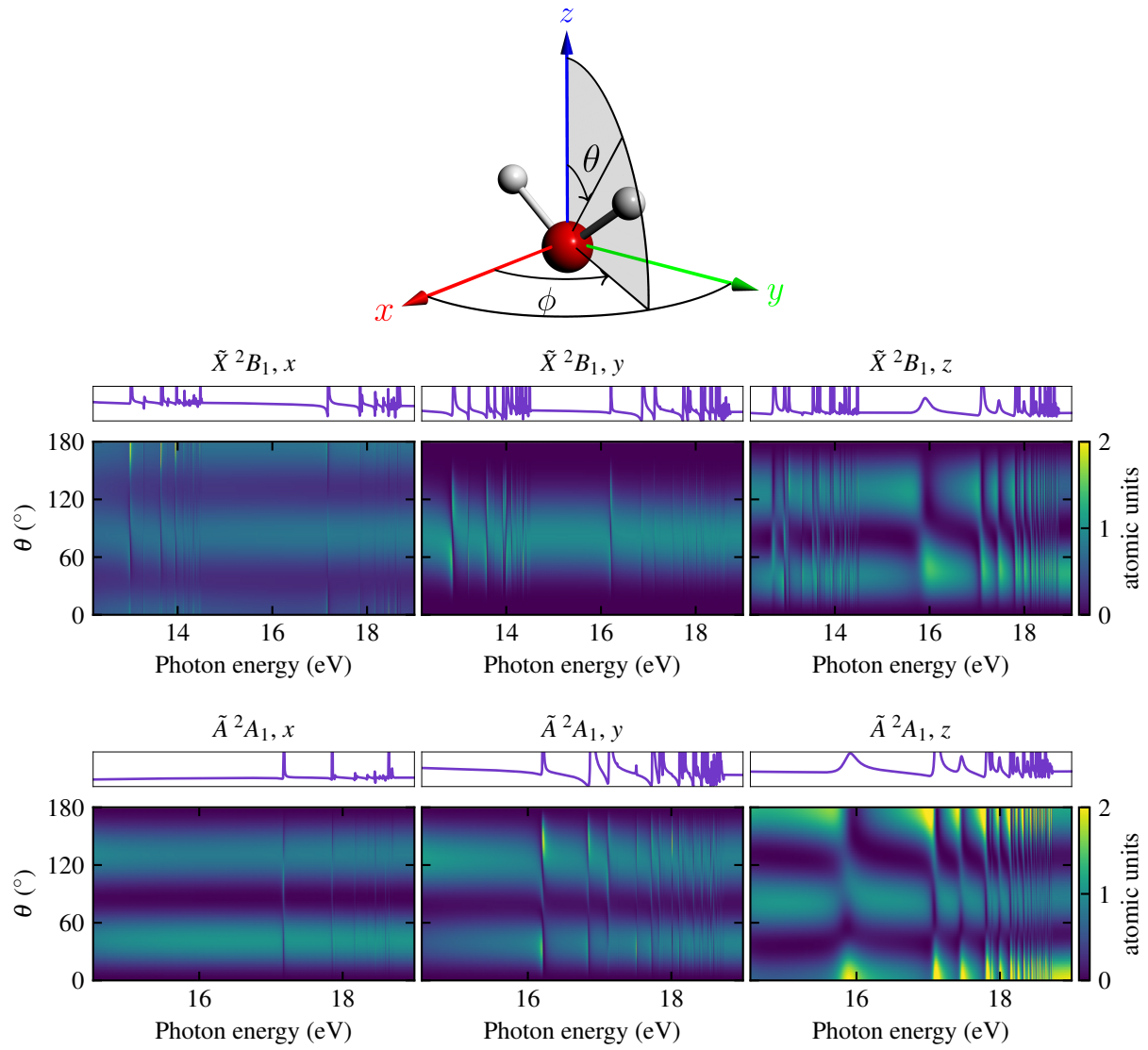

FIG. 8. Photoelectron spectra as a function of photon energy and the electron emission angle θ (referred to the molecular axis, see inset) obtained after integrating over the azimuthal angle ϕ (see inset). Top row: $\tilde{X}\,^2B_1$ channel. Bottom row: $\tilde{A}\,^2A_1$ channel. Panels from left to right: x, y and z polarizations. The corresponding θ and ϕ integrated partial cross sections are shown on top of each panel.

C. Molecular frame photoelectron angular distributions

We have also computed the MFPADs for the $\tilde{X}\,^2B_1$ and $\tilde{A}\,^2A_1$ ionization channels in the low energy region. Figure 8 shows two dimensional (2D) plots of the photoionization cross sections as a function of photon energy and the electron emission angle θ, defined with respect to the molecular axis, for the x, y and z polarization directions. We have used the following convention

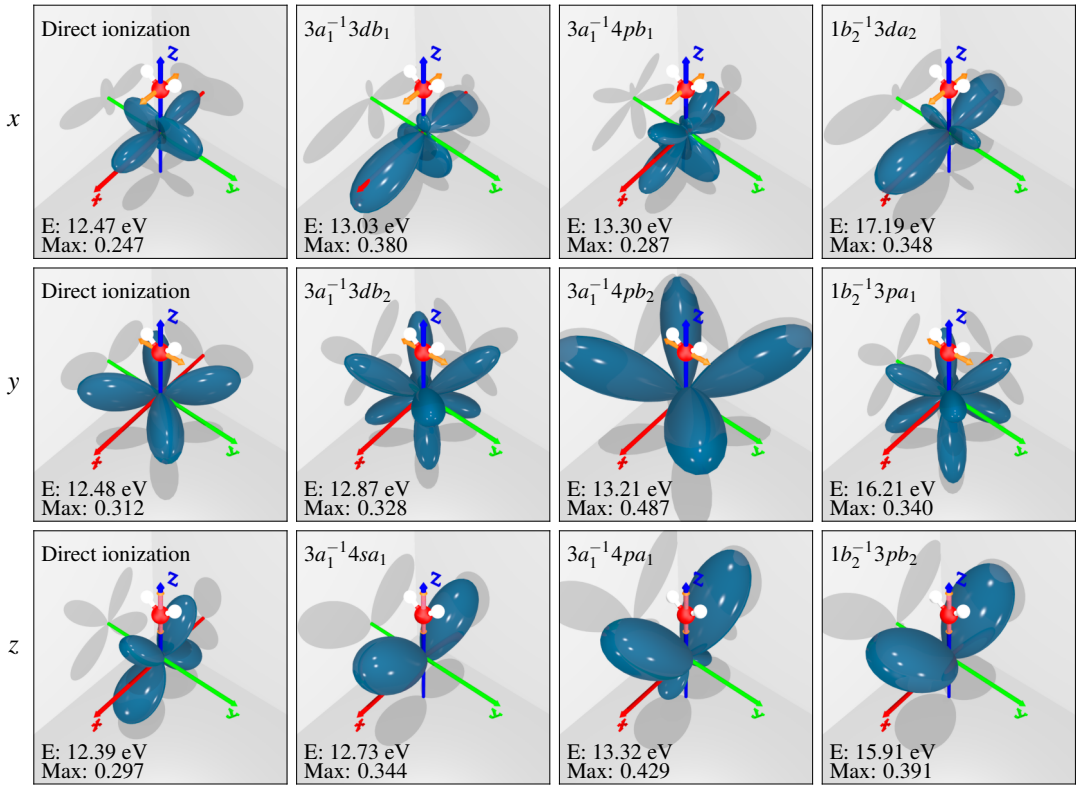

FIG. 9. MFPADs at different photon energies in the $\tilde{X}\ ^2B_1$ ionization channel. The left panels show results at photon energies E where Feshbach resonances are absent. The remaining panels show results in the vicinity of some selected resonances. Panels in each row correspond to a different polarization directions: (top) x, (middle) y and (bottom) z. For a better visualization, the MFPADs are renormalized and the maximum absolute value is given at the bottom of each panel. On top of the MFPAD surfaces, a sketch of the water molecule is shown, indicating its orientation in space. The orange double arrow indicates the polarization direction.

for cartesian directions and angles: z coincides with the molecular axis, x is perpendicular to the molecular plane yz, and y is contained in the molecular plane and is perpendicular to the molecular axis (see sketch on top of fig. 8). $\theta = 0°$ represents emission along the molecular axis in between the two O–H bonds, and $\theta = 180°$ emission along the molecular axis away of the O–H bonds. The 2D plots in fig. 8 have been obtained by integrating over the azimuthal angle ϕ. As expected, the MFPADs rapidly change with energy in the vicinity of the resonances, as already reported by Borràs *et al.*[14] for the CO molecule. This abrupt change is also evident in figs. 9 and 10, where we have depicted a few selected polar plots of MFPADs in full dimensionality, in regions where

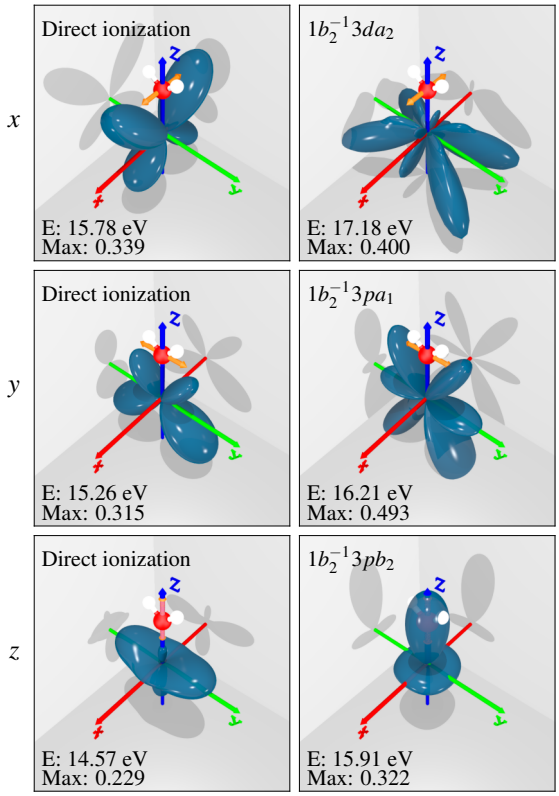

FIG. 10. Same as in fig. 9 but for the $\tilde{A}\,^2A_1$ channel.

direct non resonant ionization is dominant and where the widest resonances show up.

We first discuss our results for non resonant (direct) ionization in the $\tilde{X}\,^2B_1$ channel (top panels of fig. 8 and left panels in fig. 9). Therefore, for the time being, we will ignore the sharp changes in the MFPADs due to the presence of resonances. In the case of x polarization, fig. 8 (top left panel) shows the presence of a rather uniform background as a function of photon energy. Three bands around $\theta = 0°$, $90°$, and $180°$ can be observed. They correspond, respectively, to emission along the molecular axis z, perpendicular to it (in the molecular plane yz) and along the molecular axis z away for the O–H bonds. The shape of the MFPAD for direct ionization in fig. 9 (upper left panel) recalls that of a d_{z^2} orbital. For y polarization (middle top panel in fig. 8), one can see a central band around $90°$ denoting emission perpendicular to the molecular axis. Figure 9 (middle left panel) shows that non resonant ionization leads to emission with a d_{xy} shape. For z polarization (right top panel in fig. 8), the background exhibits two bands, one centered at $\sim 120°$ and another at $\sim 30°$, with no emission around $90°$. Therefore, electron emission occurs above and below the xy plane, as shown in fig. 9 (bottom left panel), where the MFPAD adopts a d_{xz} shape.

These uniform patterns change dramatically in the vicinity of the Feshbach resonances, where electron correlation forces electrons to escape in directions that are not the ones that one would expect by exclusively using symmetry considerations, e.g., the point-group symmetry of the electronic state in which the cation is left and that of the angular momentum l associated to the dominant partial wave. Figures 8 and 9 show that emission patterns in the vicinity of resonances are very diverse. Without going into a detailed description of all the features for all resonances, one can see, for instance, that, as one goes through the wide $1b_2^{-1}3pb_2$ resonance from below to above ~ 16 eV in the z polarization case (fig. 8, right top panel), emission at $\sim 120^\circ$ practically vanishes while emission below $\sim 60^\circ$ is strongly reinforced. This means that the bottom lobes of the non resonant MFPAD shrink and the top lobes expand, as shown in fig. 9 (bottom left and right panels). As one departs from 16 eV, the non resonant behavior is progressively recovered. Similar qualitative features repeat every time a resonance is hit at higher energies.

We now discuss the most relevant features for non resonant (direct) ionization in the $\tilde{A}\ ^2A_1$ channel (lower panels of fig. 8 and left panels in fig. 10). In the case of x polarization, the MFPAD has a d_{xz} shape with the top lobes larger than the bottom ones. This is also apparent in the background of fig. 8 (bottom left), consisting of two bands with different intensity. For y polarization, the MFPAD exhibits a d_{yz} shape, with the top lobes smaller than the bottom ones, and for z polarization, a d_z^2 shape with the lobe going along $-z$ larger than that going along $+z$. As for the $\tilde{X}\ ^2B_1$ channel, these patterns change dramatically in the vicinity of the Feshbach resonances. Focusing again on the wide $1b_2^{-1}3pb_2$ resonance, one can see (fig. 8, bottom right) that, as the resonance is crossed from below to above 16 eV, electron emission dramatically increases at around 0°, vanish at around 180° and decreases significantly at 90°, implying that the $+z$ lobe expands, the $-z$ one practically disappears and the size of the ring in the xy plane is significantly reduced (fig. 8, bottom panels) . Figure 8 (bottom right) shows that the MFPAD changes in this same way for resonances appearing at higher energy, but more abruptly as they are narrower than the $1b_2^{-1}3pb_2$ one.

V. CONCLUSIONS

We have calculated total and partial cross sections, β asymmetry parameters and molecular frame photoelectron angular distributions for outer-valence shell ($1b_1$, $3a_1$, $1b_2$) photoionization of the H_2O molecule using the XCHEM method. This method accounts for electron correlation in the electronic continuum, which is crucial to describe Feshbach resonances and their autoion-

ization decay. Although calculations have been designed to obtain an accurate representation of photoionization in the energy region between the first and the third ionization thresholds of the molecule, where a large number of Feshbach resonances can be reached, comparison with total and partial cross sections available in the literature at higher energies is quite satisfactory. We have identified a large number of Feshbach resonances, some of them previously unknown, in the region between 12.2–18.7 eV, for which we provide energy positions and widths. Many of these resonances lead to pronounced peaks in the photoionization spectra, some of them remarkably wide (up to 0.2 eV, for resonances converging to the third ionization threshold), which should be observable in high-energy resolution experiments. We have shown that, in the vicinity of these peaks, both asymmetry parameters and MFPADs vary very rapidly with photoelectron energy, which is the consequence of the interference between the direct ionization and autoionization processes. These interferences lead to dramatic changes in the preferred electron emission directions in comparison with non resonant (direct) photoionization, and are mainly governed by electron correlation in the ionization continuum. We hope that the present work will spur experimental measurements in this energy region, which is the usual one that can be reached with current XUV single attosecond pulses or trains of attosecond pulses.

ACKNOWLEDGMENTS

We thank Prof. Luca Argenti for technical support and very valuable discussions for the evaluation of molecular-frame photoelectron angular distributions. All calculations were performed at the Mare Nostrum Supercomputer of the Red Española de Supercomputación (BSC-RES) and the Centro de Computación Científica de la Universidad Autónoma de Madrid (CCC-UAM). Work supported by European COST Action CA18222 AttoChem, the projects PDC2021-121073-I00, PID2019-105458RB-I00 and PID2019-106732GB-I00 funded by MCIN/ AEI /10.13039/501100011033 and by the European Union "NextGenerationEU"/PRTRMICINN programs, the "Severo Ochoa" Programme for Centres of Excellence in R&D (CEX2020-001039-S), and the "María de Maeztu" Programme for Units of Excellence in R&D (CEX2018-000805-M).

REFERENCES

[1]M. Nisoli, P. Decleva, F. Calegari, A. Palacios, and F. Martín, Chemical Reviews **117**, 10760 (2017).

[2]H. N. Varambhia and J. Tennyson, J. Phys. B: At. Mol. Opt. Phys. **40**, 1211 (2007).

[3]D. S. Brambila, A. G. Harvey, Z. Mašín, J. D. Gorfinkiel, and O. Smirnova, J. Phys. B: At. Mol. Opt. Phys. **48**, 245101 (2015), publisher: IOP Publishing.

[4]V. P. Majety, A. Zielinski, and A. Scrinzi, New J. Phys. **17**, 063002 (2015), publisher: IOP Publishing.

[5]V. P. Majety and A. Scrinzi, Phys. Rev. Lett. **115**, 103002 (2015), publisher: American Physical Society.

[6]D. Toffoli and P. Decleva, J. Chem. Theory Comput. **12**, 4996 (2016), publisher: American Chemical Society.

[7]C. Marante, M. Klinker, I. Corral, J. González-Vázquez, L. Argenti, and F. Martín, Journal of Chemical Theory and Computation **13**, 499 (2017), publisher: American Chemical Society.

[8]F. Martín, J. González-Vuez, I. Corral, J. V. Borrs, M. Klinker, L. Argenti, and C. Marante, (2023), `https://doi.org/10.21950/GHWTML`.

[9]C. Marante, M. Klinker, T. Kjellsson, E. Lindroth, J. González-Vázquez, L. Argenti, and F. Martín, Physical Review A **96**, 022507 (2017), publisher: American Physical Society.

[10]L. Barreau, C. L. M. Petersson, M. Klinker, A. Camper, C. Marante, T. Gorman, D. Kiesewetter, L. Argenti, P. Agostini, J. González-Vázquez, P. Salières, L. F. DiMauro, and F. Martín, Phys. Rev. Lett. **122**, 253203 (2019), publisher: American Physical Society.

[11]R. Y. Bello, V. J. Borràs, J. González-Vázquez, and F. Martín, Phys. Rev. Research **4**, 043028 (2022), publisher: American Physical Society.

[12]M. Klinker, C. Marante, L. Argenti, J. González-Vázquez, and F. Martín, The Journal of Physical Chemistry Letters **9**, 756 (2018), publisher: American Chemical Society.

[13]S. M. Poullain, M. Klinker, J. González-Vázquez, and F. Martín, Phys. Chem. Chem. Phys. **21**, 16497 (2019), publisher: The Royal Society of Chemistry.

[14]V. J. Borràs, J. González-Vázquez, L. Argenti, and F. Martín, J. Chem. Theory Comput. **17**, 6330 (2021), publisher: American Chemical Society.

[15]B. C. Garrett, D. A. Dixon, D. M. Camaioni, D. M. Chipman, M. A. Johnson, C. D. Jonah, G. A. Kimmel, J. H. Miller, T. N. Rescigno, P. J. Rossky, S. S. Xantheas, S. D. Colson, A. H.

Laufer, D. Ray, P. F. Barbara, D. M. Bartels, K. H. Becker, K. H. J. Bowen, S. E. Bradforth, I. Carmichael, J. V. Coe, L. R. Corrales, J. P. Cowin, M. Dupuis, K. B. Eisenthal, J. A. Franz, M. S. Gutowski, K. D. Jordan, B. D. Kay, J. A. LaVerne, S. V. Lymar, T. E. Madey, C. W. McCurdy, D. Meisel, S. Mukamel, A. R. Nilsson, T. M. Orlando, N. G. Petrik, S. M. Pimblott, J. R. Rustad, G. K. Schenter, S. J. Singer, A. Tokmakoff, L.-S. Wang, and T. S. Zwier, Chem. Rev. **105**, 355 (2005), publisher: American Chemical Society.

[16]E. Alizadeh, T. M. Orlando, and L. Sanche, Annual Review of Physical Chemistry **66**, 379 (2015), _eprint: https://doi.org/10.1146/annurev-physchem-040513-103605.

[17]P. Gürtler, V. Saile, and E. E. Koch, Chemical Physics Letters **51**, 386 (1977).

[18]C. M. Truesdale, S. Southworth, P. H. Kobrin, D. W. Lindle, G. Thornton, and D. A. Shirley, J. Chem. Phys. **76**, 860 (1982), publisher: American Institute of Physics.

[19]M. S. Banna, B. H. McQuaide, R. Malutzki, and V. Schmidt, J. Chem. Phys. **84**, 4739 (1986), publisher: American Institute of Physics.

[20]K. H. Tan, C. E. Brion, P. E. Van der Leeuw, and M. J. van der Wiel, Chemical Physics **29**, 299 (1978).

[21]C. E. Brion and F. Carnovale, Chemical Physics **100**, 291 (1985).

[22]M. Huppert, I. Jordan, D. Baykusheva, A. von Conta, and H. J. Wörner, Phys. Rev. Lett. **117**, 093001 (2016).

[23]X. Gong, S. Heck, D. Jelovina, C. Perry, K. Zinchenko, R. Lucchese, and H. J. Wörner, Nature **609**, 507 (2022), number: 7927 Publisher: Nature Publishing Group.

[24]G. H. F. Diercksen, W. P. Kraemer, T. N. Rescigno, C. F. Bender, B. V. McKoy, S. R. Langhoff, and P. W. Langhoff, J. Chem. Phys. **76**, 1043 (1982), publisher: American Institute of Physics.

[25]S. Engin, J. González-Vázquez, G. G. Maliyar, A. R. Milosavljević, T. Ono, S. Nandi, D. Iablonskyi, K. Kooser, J. D. Bozek, P. Decleva, E. Kukk, K. Ueda, and F. Martín, Structural Dynamics **6**, 054101 (2019), publisher: American Institute of Physics.

[26]J. Benda, J. D. Gorfinkiel, Z. Mašín, G. S. J. Armstrong, A. C. Brown, D. D. A. Clarke, H. W. van der Hart, and J. Wragg, Phys. Rev. A **102**, 052826 (2020), publisher: American Physical Society.

[27]T. Moitra, A. Ponzi, H. Koch, S. Coriani, and P. Decleva, J. Phys. Chem. Lett. **11**, 5330 (2020), publisher: American Chemical Society.

[28]M. Rubio, L. Serrano-Andrés, and M. Merchán, J. Chem. Phys. **128**, 104305 (2008), publisher: American Institute of Physics.

[29]G. Theodorakopoulos, I. D. Petsalakis, and M. S. Child, J. Phys. B: At. Mol. Opt. Phys. **29**, 4543 (1996), publisher: IOP Publishing.

[30]M. S. Child and C. Jungen, J. Chem. Phys. **93**, 7756 (1990), publisher: American Institute of Physics.

[31]M. J. J. Vrakking, Y. T. Lee, R. D. Gilbert, and M. S. Child, J. Chem. Phys. **98**, 1902 (1993), publisher: American Institute of Physics.

[32]F. Martín, Journal of Physics B: Atomic, Molecular and Optical Physics **32**, R197 (1999).

[33]L. Cattaneo, J. Vos, R. Y. Bello, A. Palacios, S. Heuser, L. Pedrelli, M. Lucchini, C. Cirelli, F. Martín, and U. Keller, Nature Physics **14**, 733 (2018).

[34]C. Marante, L. Argenti, and F. Martín, Physical Review A **90**, 012506 (2014), publisher: American Physical Society.

[35]H.-J. Werner, P. J. Knowles, G. Knizia, F. R. Manby, and M. Schütz, WIREs Computational Molecular Science **2**, 242 (2012), _eprint: https://onlinelibrary.wiley.com/doi/pdf/10.1002/wcms.82.

[36]T. H. Dunning, J. Chem. Phys. **90**, 1007 (1989), publisher: American Institute of Physics.

[37]A. W. Potts and W. C. Price, Proceedings of the Royal Society of London. A. Mathematical and Physical Sciences **326**, 181 (1972), publisher: Royal Society.

[38]C. R. Brundle, D. W. Turner, and W. C. Price, Proceedings of the Royal Society of London. Series A. Mathematical and Physical Sciences **307**, 27 (1968), publisher: Royal Society.

[39]D. H. Katayama, R. E. Huffman, and C. L. O'Bryan, J. Chem. Phys. **59**, 4309 (1973), publisher: American Institute of Physics.

[40]G. N. Haddad and J. A. R. Samson, J. Chem. Phys. **84**, 6623 (1986), publisher: American Institute of Physics.

[41]A. U. Hazi, Phys. Rev., A; (United States) **19:2** (1979), 10.1103/PhysRevA.19.920, institution: Theoretical Atomic and Molecular Physics Group, Lawrence Livermore Laboratory, University of California, Livermore, California 94550.

[42]P. Gürtler, V. Saile, and E. E. Koch, Chemical Physics Letters **48**, 245 (1977).

[43]W. B. Peatman, B. Gotchev, P. Gürtler, E. E. Koch, and V. Saile, J. Chem. Phys. **69**, 2089 (1978), publisher: American Institute of Physics.

[44]A. C. Parr, D. L. Ederer, B. E. Cole, J. B. West, R. Stockbauer, K. Codling, and J. L. Dehmer, Phys. Rev. Lett. **46**, 22 (1981), publisher: American Physical Society.

[45]P. M. Dehmer, P. J. Miller, and W. A. Chupka, J. Chem. Phys. **80**, 1030 (1984), publisher: American Institute of Physics.

[46]K. P. Huber, G. Stark, and K. Ito, J. Chem. Phys. **98**, 4471 (1993), publisher: American Institute of Physics.